

THE MAGNETIC LANDSCAPE OF THE SUN'S POLAR REGION

S. TSUNETA,¹ K. ICHIMOTO,¹ Y. KATSUKAWA,¹ B. W. LITES,² K. MATSUZAKI,³ S. NAGATA,⁴ D. OROZCO SUÁREZ,⁵
T. SHIMIZU,³ M. SHIMOJO,⁶ R. A. SHINE,⁷ Y. SUEMATSU,¹ T. K. SUZUKI,⁸ T. D. TARBELL,⁷ AND A. M. TITTLE⁷

Received 2007 November 9; accepted 2008 August 1

ABSTRACT

We present observations of the magnetic landscape of the polar region of the Sun that are unprecedented in terms of spatial resolution, field of view, and polarimetric precision. They were carried out with the Solar Optical Telescope aboard *Hinode*. Using a Milne-Eddington inversion, we find many vertically oriented magnetic flux tubes with field strengths as strong as 1 kG scattered in latitude between 70° and 90°. They all have the same polarity, consistent with the global polarity of the polar region. The field vectors are observed to diverge from the centers of the flux elements, consistent with a view of magnetic fields that are expanding and fanning out with height. The polar region is also found to have ubiquitous horizontal fields. The polar regions are the source of the fast solar wind, which is channeled along unipolar coronal magnetic fields whose photospheric source is evidently rooted in the strong-field, vertical patches of flux. We conjecture that vertical flux tubes with large expansion around the photospheric-coronal boundary serve as efficient chimneys for Alfvén waves that accelerate the solar wind.

Subject headings: solar wind — Sun: faculae, plages — Sun: magnetic fields — Sun: photosphere

1. INTRODUCTION

The Sun's polar magnetic fields are thought to be a direct manifestation of the global poloidal fields in the interior, which serve as seed fields for the global dynamo that produces the toroidal fields responsible for active regions and sunspots. The polar regions are also the source of the fast solar wind. Although the polar regions are of crucial importance to the dynamo process and the acceleration of the fast solar wind, their magnetic properties are poorly known. Magnetic field measurements in the solar polar regions have long been a challenge: variable seeing, combined with a strong intensity gradient and the foreshortening effect at the solar limb, greatly increases the systematic noise in ground-based magnetograms. Nevertheless, pioneering observations have been carried out for the polar regions (Tang & Wang 1991; Lin et al. 1994; Homann et al. 1997; Okunev 2004; Okunev & Kneer 2004; Blanco Rodriguez et al. 2007). These observations typically have provided measurements only of the line-of-sight magnetic component. Full Stokes polarimetry has also been carried out, but as with most of the ground-based observations mentioned above, the spatial resolution of these measurements was limited by seeing (Lites 1996). Another limitation of past polar observations is that they have been restricted to individual polar faculae within a small field of view and have not provided us with a global magnetic landscape of the polar region, except for the Global Oscillation Network Group and SOLIS (Harvey et al. 2007).

We have investigated the properties of the photospheric magnetic field in the polar regions using the Solar Optical Telescope, SOT (Tsuneta et al. 2008; Suematsu et al. 2008; Ichimoto et al. 2008; Shimizu et al. 2008). SOT is a diffraction-limited (0.2''–0.3'')

Gregorian telescope with filtergraph and spectropolarimeter aboard the satellite *Hinode* (Kosugi et al. 2007). These observations are unprecedented in terms of their very high spatial resolution, wide field of view, and high polarimetric sensitivity and accuracy in measurements of vector magnetic fields.

2. STOKES MAPS OF THE POLAR REGION

Hinode observed the solar polar region on 2007 March 16, when the south pole was located 7° inside the visible solar disk. Stokes profiles of two Fe I lines (630.2 and 630.3 nm) were observed with the spectropolarimeter (SP) of SOT. The degrees of linear (Stokes Q and U) and circular (Stokes V) polarization are defined as

$$\frac{\int Q(\lambda)d\lambda}{I_c \int d\lambda}, \quad \frac{\int U(\lambda)d\lambda}{I_c \int d\lambda}, \quad \frac{\int |V(\lambda)|d\lambda}{I_c \int d\lambda},$$

respectively, where I_c is the continuum intensity and Q , U , and V are the observed Stokes profiles. The SP wavelength sampling is 2.15 pm. When the red lobe of the Stokes V profile is positive, a minus sign is added, meaning that the line-of-sight field is directed away from the observer. The integrations are performed between -21.6 and -4.32 pm and between $+4.32$ and $+21.6$ pm from the center of individual Stokes I profiles. These wavelength ranges were determined by examining the actual data. If the range is too wide, the maps will be more susceptible to photon noise. Maps of these degrees of polarization are hereafter called the Stokes Q , U , and V maps and are shown in Figure 1. These data were taken at 12:02:19–14:55:48 UT on 2007 March 16.

Position angles for Stokes Q and U were determined as follows: 0° runs from east to west, and 90° is north-south. If the transverse field is directed to the west, it will be seen as white in the Stokes Q map, and if it is directed north it will be black. If the transverse field is directed at 45°, it will be seen as white in the Stokes U map, with black denoting 135°. Black (positive polarity) in the Stokes V map indicates that the magnetic field is directed toward the observer, and white (negative polarity) is directed away from the observer.

We noticed scattered isolated patches in the Stokes Q map (Fig. 1b). They coherently have negative values (*black*), indicating

¹ National Astronomical Observatory, Mitaka, Tokyo 181-8588, Japan.
² High Altitude Observatory, National Center for Atmospheric Research, Boulder, CO 80307-3000.
³ ISAS/JAXA, Sagami-hara, Kanagawa 229-8510, Japan.
⁴ Kwasan and Hida Observatories, Kyoto University, Yamashina, Kyoto 607-8471, Japan.
⁵ Instituto de Astrofísica de Andalucía, CSIC, E-18008 Granada, Spain.
⁶ Nobeyama Solar Radio Observatory, National Astronomical Observatory of Japan, Nobeyama, Nagano 284-1305, Japan.
⁷ Lockheed Martin Solar and Astrophysics Laboratory, Palo Alto, CA 94304.
⁸ School of Arts and Sciences, University of Tokyo, Meguro, Tokyo 153-8902, Japan.

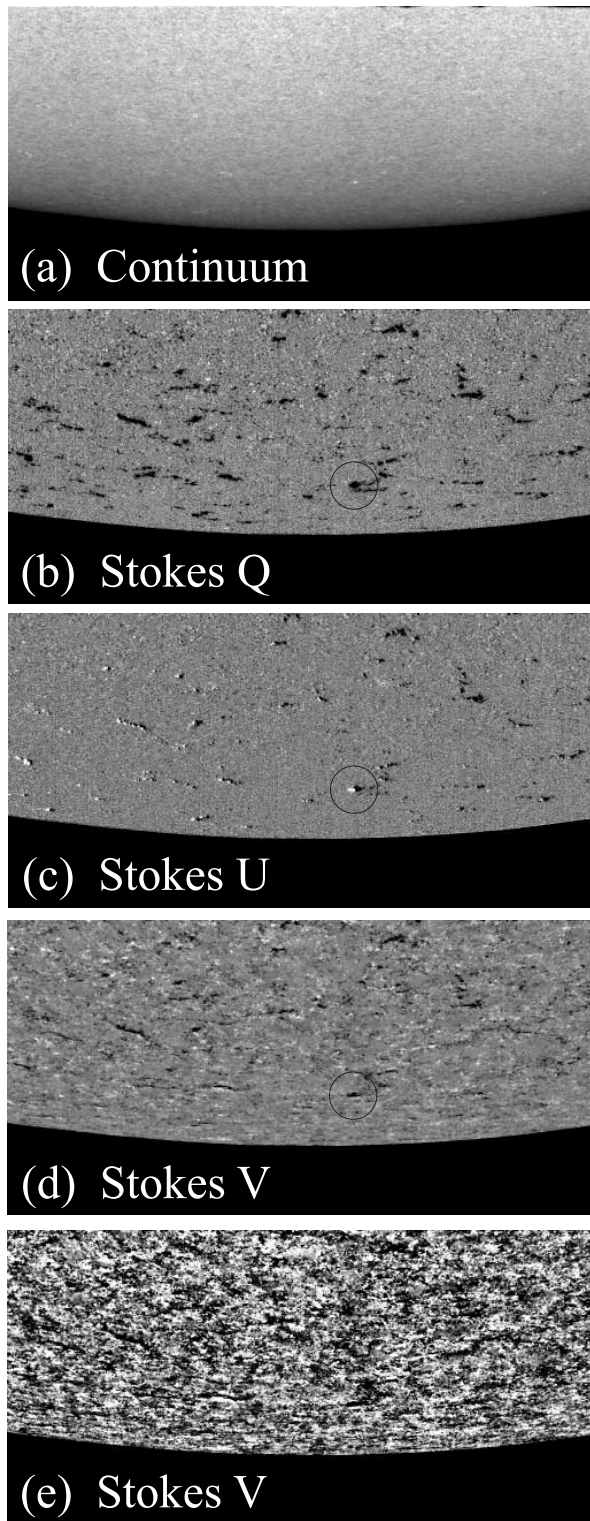


FIG. 1.—Polarization maps of the south polar region taken at 12:02:19–14:55:48 UT on 2007 March 16. (a) Continuum map; (b) Stokes Q map (transverse magnetic field); (c) Stokes U map (transverse magnetic field); (d, e) Stokes V maps (line-of-sight magnetic field). East is to the left, and north is up. The gray scale indicates the wavelength-integrated total degree of polarization. The images saturate at a degree of polarization of ± 0.003 for (b), (c), and (e), and at ± 0.02 for (d). Black circles in (b), (c), and (d) indicate one fanning-out magnetic structure.

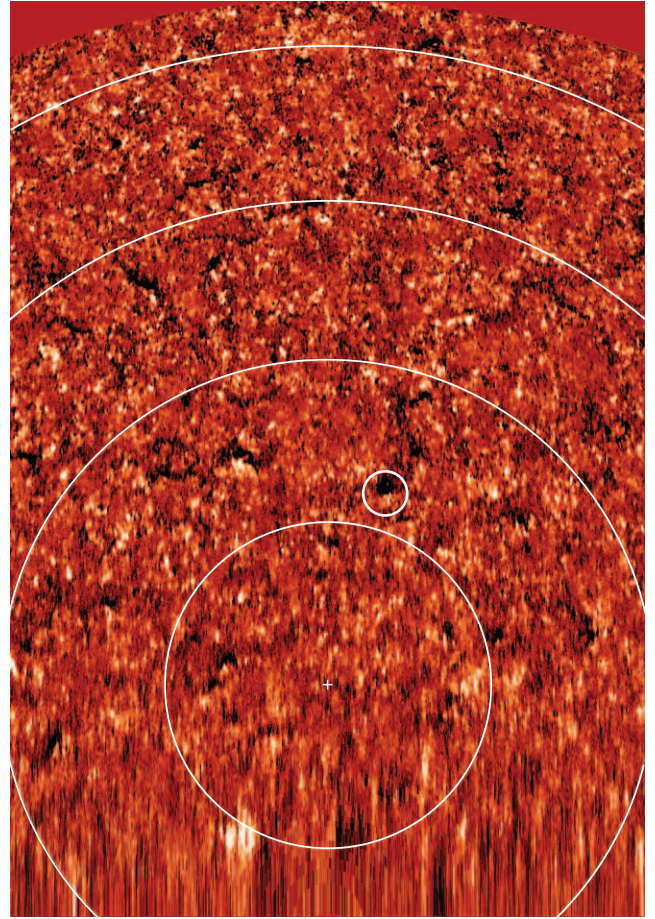


FIG. 2.—Polar view of the circular polarization (Stokes V) signal, created from Figs. 1d and 1e. The original observing field of view (Fig. 1) is $327.52''$ (east-west) by $163.84''$ (north-south) and was converted to a map seen from above the south pole. East is to the left, west is to the right, and the observation was carried out from the top down. Spatial resolution is lost near the extreme limb (i.e., near the bottom of the figure). The field of view is $327.52''$ (east-west) by $472.96''$ (north-south along the line of sight). The field of view for the line-of-sight direction ($163.84''$) expands to $472.96''$ as a result of correction for foreshortening. The pixel size is $0.16''$. Latitudinal lines for 85° , 80° , 75° , and 70° are shown as large circles, while the plus sign marks the south pole. The image saturates at a degree of polarization of ± 0.005 . Black indicates the magnetic field component toward the observer, while white is that away from the observer. The small circle indicates the same magnetic patch highlighted in Fig. 1.

the presence of a magnetic component vertical (i.e., north-south) to the local surface. These patches are associated with bipolar structures in the Stokes U map (Fig. 1c). Figures 1d and 1e show the Stokes V map. The same Stokes V image seen from just above the south pole is shown in Figure 2, where the foreshortening effect has been corrected. All the pixels in the observing coordinate (as shown in Fig. 1) are mapped to the corresponding positions in the polar maps (Figs. 2 and 3), and the gaps between the mapped pixels are interpolated. Figures 1d and 2 show a bipolar structure corresponding to the patches seen in the Stokes Q and U maps at higher latitudes. One example is indicated by a small circle in Figures 1 and 2. The bipolar structure in the Stokes V map together with the Q and U maps suggests the presence of fanning-out flux tubes vertical to the local surface.

Unipolar patches with positive polarity (*black*) are dominant at lower latitudes in the Stokes V map. This is because the vertical flux tubes located at lower latitudes have all their fanning-out magnetic vectors directed toward the observer. The dominant black polarity indicates a component of the field oriented toward the observer. This shows that all the vertical magnetic patches

are coherently directed away from the Sun, consistent with the general polar fields in 2007 (see Gopalswamy et al. 2003; Durrant et al. 2004).

We also noticed in the Stokes U map that the positive polarity (*white*) in the bipolar structures is more dominant on the east side, while negative polarity (*black*) dominates in the west. Since the flux tubes vertical to the local surface on the east side tilt toward the plus axis of Stokes U , the bipolar structures on the east side are more plus-biased (*white*), and vice versa. This explains the east-west asymmetry of the bipolar structures in the Stokes U map.

3. POLAR LANDSCAPE

3.1. Milne-Eddington Fitting

We applied a least-squares fit to the observed Fe I 630.15 nm and Fe I 630.12 nm Stokes profiles, assuming a Milne-Eddington atmosphere, with the MILOS code (Orozco Suárez et al. 2007a, 2007b). The 10 free parameters are the three components describing the vector magnetic field (strength B , inclination angle γ , and azimuth angle χ), the line-of-sight velocity, two parameters describing the source function, the ratio of line to continuum absorption coefficients, the Doppler width, the damping parameter, and the stray-light factor α . To minimize the influence of noise, we analyzed only pixels whose polarization-signal peaks exceed a given threshold above the noise level σ . The noise level was determined in the continuum wavelength range of the profiles. The fitting was performed for pixels whose Q , U , or V signal is larger than 5σ . It turns out that 10.5% of the area meets this criterion.

There may be unresolved magnetic elements along the line of sight, for example, rays passing obliquely through vertical flux tubes observed close to the limb. A nonzero stray-light factor α may be interpreted as a parameter that includes both the filling factor of a nonmagnetized or weakly magnetized atmosphere along the line of sight and the stray-light contamination factor. The stray-light profile is evaluated individually for each pixel as the average of the Stokes I profiles observed in a $1''$ wide box centered on the pixel (Orozco Suárez et al. 2007b). This arrangement also allows us to accurately estimate the stray-light profiles of rapidly changing continuum intensity toward the limb. If the stray-light contamination is negligible, then the effective filling factor of the magnetic atmosphere will be given by $f = 1 - \alpha$.

The results of our inversions applied to the polar region show that the distribution of the effective filling factor has a broad peak at $f = 0.15$ with FWHM range $0.05 < f < 0.35$ (see Fig. 5d below). Orozco Suárez et al. (2007b) suggested that there is a considerable stray-light contribution and that the actual filling factor may be larger than the nominal values derived above. As an extreme case, we also estimate the magnetic flux assuming $f = 1$ in the subsequent sections.

3.2. Vertical Kilogauss Patches and Horizontal Field

Figure 3 is a map of the magnetic field strength as seen from just above the south pole. Such a polar representation is needed to correctly see the spatial extent and size distribution of the magnetic islands in the polar region. While many of them are isolated, and some have the form of a chain of islands, complex internal structures are seen inside the individual patches. Many of the patchy magnetic islands have very high field strengths, reaching over 1 kG. These kilogauss patches coincide in position with those seen in Figure 1: they are coherently unipolar, and like plage and network fields at lower latitudes (Martínez Pillet et al. 1997), their magnetic fields are vertical to the local surface. The fanning-out structure is confirmed in the vector magnetic field map obtained from the least-squares fitting.

We notice a clear tendency for patches to be larger in size with increasing latitude, being as large as $5'' \times 5''$ at higher latitudes and $1'' \times 1''$ at lower latitudes. Degradation in spatial resolution due to the projection effect may contribute to the larger sizes at high latitude. This, however, would imply that close to the solar limb, we are observing flux tubes higher in the atmosphere. The response function to temperature (del Toro Iniesta 2003) for the core of the Stokes I profile has a broad peak between 100 and 500 km above a continuum optical depth of unity in Sun-center observations. The response function for a plane-parallel atmosphere viewed obliquely at an angle of 80° has a peak that is 50–100 km higher, implying that we are observing higher altitude atmosphere at 80° .

We are interested in the inclination angle i of the magnetic field vector with respect to the local normal. Close to the limb, it is possible to determine i without the usual 180° ambiguity (del Toro Iniesta 2003) in the transverse field components: the inclination angle is given by $\cos i = \cos \gamma \cos \theta + \sin \gamma \sin \theta \cos(\pi/2 - \chi)$, where θ is the latitude, γ is the inclination of the magnetic field vector, and χ is the azimuth angle. Figure 4 shows the inclination of the field lines: red contours indicate regions where the local inclination i is smaller than 25° (vertical), while blue contours show regions with local inclination larger than 65° (horizontal). All the large patches have fields that are vertical to the local surface (*red*), while the smaller patches tend to be horizontal (*blue*). Most of the magnetic structures seen in Figure 3 thus have either vertical or horizontal direction. These two types do not appear to be spatially correlated.

Figure 4 also indicates that magnetic patches of larger spatial size coincide in position with polar faculae (Lin et al. 1994; Okunev 2004; Okunev & Kneer 2004). Figure 5c shows histograms of the continuum intensity relative to the local average intensity for pixels with magnetic field strength greater than 300 and 800 G. The distribution of the horizontal fields is essentially symmetric about the average intensity, while the vertical fields tend to have higher continuum intensities. These bright points correspond to the polar faculae. The vertical kilogauss patches change considerably in shape and distribution over 5–10 hr, while the spatial distribution of the horizontal magnetic field changes completely in 30 minutes or less. This is consistent with the observations of the horizontal fields made by SOLIS (Harvey et al. 2007) and *Hinode* (Centeno et al. 2007; Ishikawa et al. 2008).

We manually selected 41 patches with vertical magnetic field to derive the distribution of magnetic flux and patch size as a function of latitude. The total magnetic flux of a magnetic patch is estimated as $\sum_i B_i f_i s_i$, where B_i and f_i are the intrinsic magnetic field strength and filling factor of the i th SOT pixel inside the patch, respectively, and s_i is the common pixel size. The magnetic flux of the patches ranges from 1.8×10^{18} to 1.0×10^{20} Mx, with mean flux of 2.7×10^{19} Mx. We obtain the size of the magnetic patches as $\sum_i s_i$, where the summation is over pixels with per-pixel average field strength $B_i f_i$ larger than 10 G: The size increases by a factor of 1.92, and the flux $\sum_i B_i f_i s_i$ decreases by a factor of 1.33 between latitudes 70° and 85° . The total magnetic flux is preserved to within 40%.

Figure 5a shows a histogram (probability distribution function, PDF) of the intrinsic magnetic field strength B for latitudes above 75° : vertical magnetic fields with inclination $i < 25^\circ$ dominate the stronger field regime, while horizontal fields with $i > 65^\circ$ are much more prevalent below 250 G. Of the pixels for which the inversion was performed, 41% contained vertical magnetic field, and 49% horizontal magnetic field. Figure 5a can be compared with the PDF for the quiet Sun obtained with *Hinode* by Orozco Suárez et al. (2007b, Fig. 7). A magnetic energy PDF, defined by

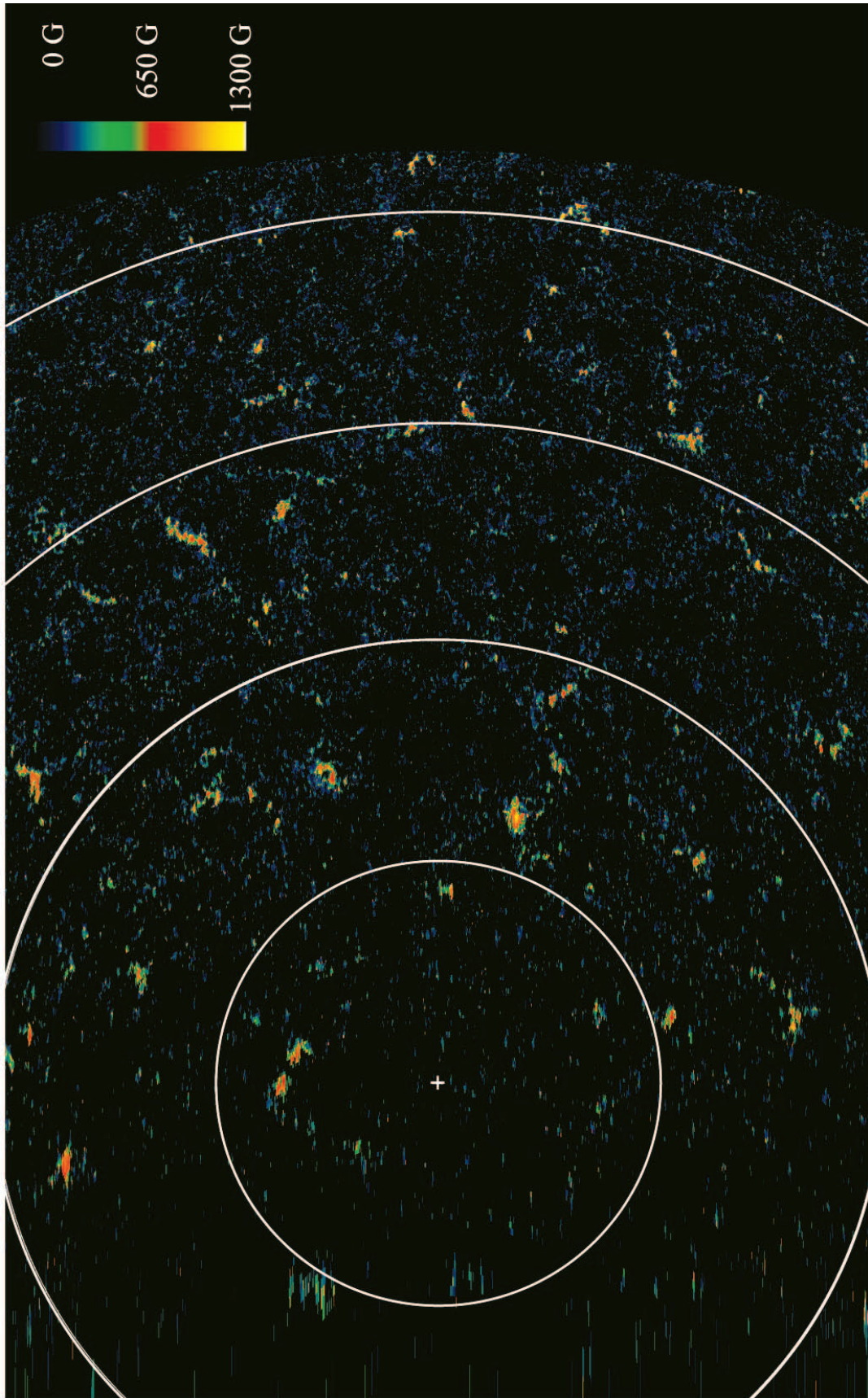


FIG. 3.— South polar view of the magnetic field strength taken at 12:02:19–14:55:48 UT on 2007 March 16. The dimensions and orientation are the same as in Fig. 3. The magnetic field strength is obtained for pixels meeting a given threshold (see text).

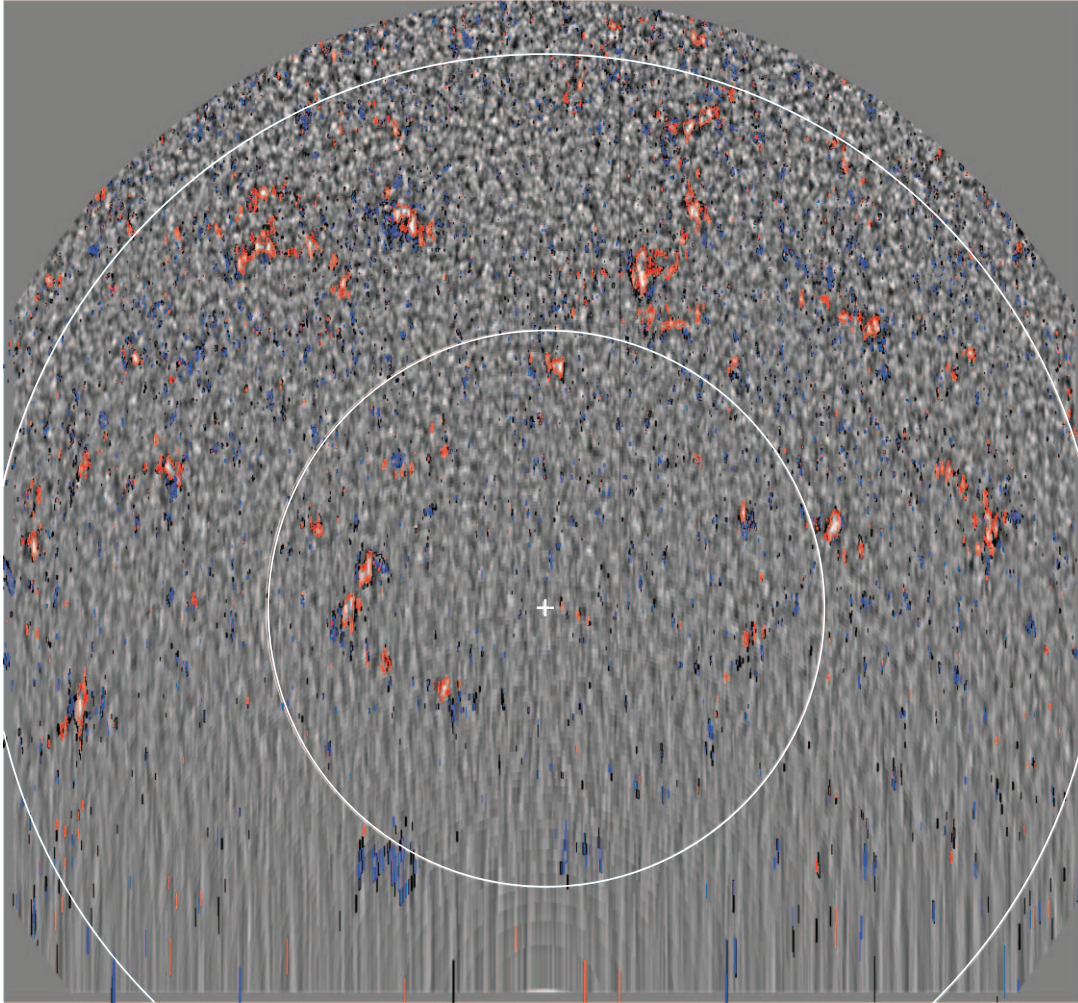


FIG. 4.— Polar view in the continuum for latitudes above 80° , created from Fig. 1*a*. Colored contours indicate locations with average field strength Bf of 200 G. (The region inside the contour has average field strength larger than 200 G.) Red indicates regions where the local inclination $i < 25^\circ$ (vertical), while blue shows regions $i > 65^\circ$ (horizontal). East is to the left, and west is to the right. Latitudinal lines for 85° and 80° are shown, with the plus sign indicating the south pole. Near the extreme limb (to the bottom), spatial resolution is lost.

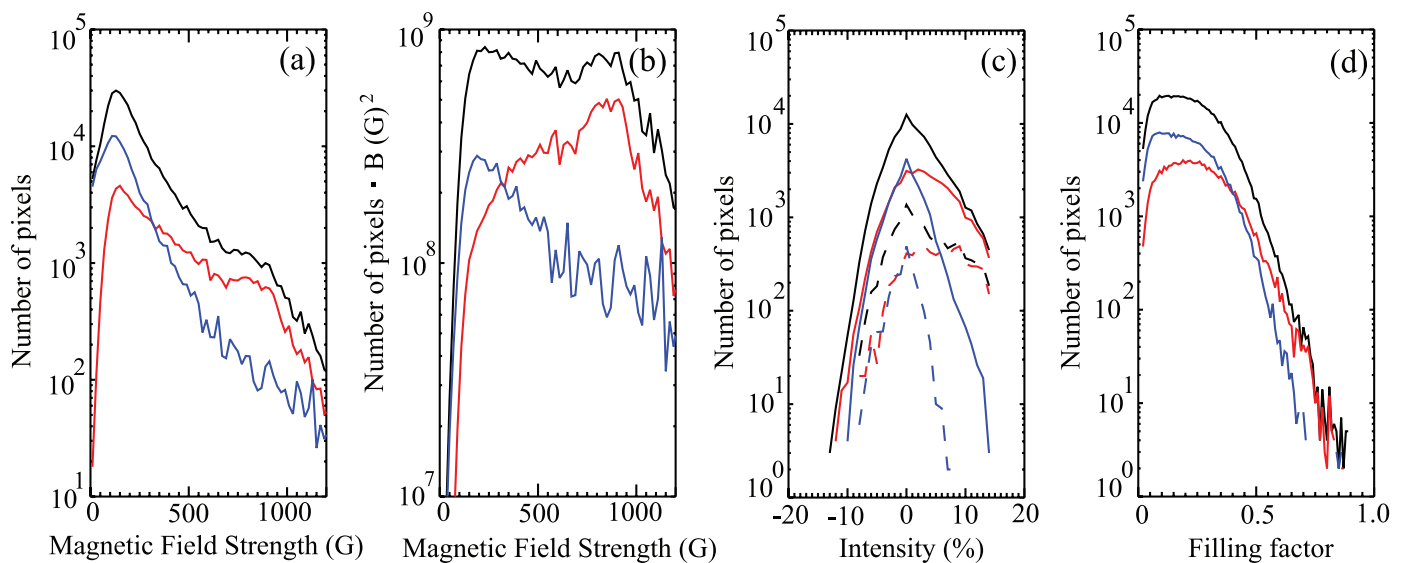


FIG. 5.— (a) Number of pixels as a function of magnetic field strength (probability distribution function). Red lines indicate the vertical field, blue the horizontal field, and black the total. (b) Number of pixels times B^2 as a function of magnetic field strength. The bin size for the magnetic field strength in (a) and (b) is 20 G. (c) Histograms of continuum intensity for magnetic field strengths above 300 G (solid lines) and 800 G (dashed lines). Since the continuum intensity rapidly decreases toward the limb, the horizontal axis is the normalized excess continuum level with respect to the continuum averaged over a $6.4''$ box. (d) Filling factor as defined in § 3.1. All panels are for latitudes above 75° .

the number of pixels multiplied by B^2 , as a function of field strength is shown in Figure 5b. This illustrates where the magnetic energy is mainly located as a function of field strength. The vertical flux tubes with higher field strength are energetically dominant, while weaker horizontal flux tubes, by contrast, carry more energy.

3.3. Total Magnetic Flux in the Polar Region

The total *vertical* magnetic flux in the SOT field of view is 2.2×10^{21} Mx, while the total *horizontal* flux is 4.0×10^{21} Mx. The effective filling factor was taken into account in estimating these total fluxes: the flux of an individual pixel in Figure 3 is estimated as Bf times the pixel size, with foreshortening correction.

Considering the stray-light contribution, the actual filling factor may be larger than the nominal values derived with the least-squares fit. As an extreme case, we estimate the magnetic flux assuming $f = 1$: the total *vertical* magnetic flux then becomes 9.9×10^{21} Mx, and the total *horizontal* magnetic flux becomes 2.0×10^{22} Mx. The differences are factors of 0.22 and 0.2, which roughly correspond to the average filling factor for the vertical and horizontal fields, respectively. If the contribution from stray light reaches 50% (Orozco Suárez et al. 2007b), the total *vertical* flux is estimated to be 7.2×10^{21} Mx. Note that we have to be careful in comparing the horizontal magnetic flux with the vertical flux because of the different sensitivity in the degree of Stokes Q , U , and V polarization to the transverse and line-of-sight magnetic fields.

Since the inversion was performed for only the 10.5% of pixels with high signal-to-noise ratio and the horizontal field strength is generally smaller than the vertical, we also obtained the horizontal magnetic flux from the wavelength-integrated Stokes V signals using a weak-field approximation. This should be less sensitive to error. We excluded pixels with flux lower than 3σ (7.2 Mx cm^{-2}), performed foreshortening correction in the pixel size, and added a correction (a factor of $\sqrt{2}$) for the transverse horizontal fields unseen in Stokes V . The total horizontal flux thus obtained is 4.35×10^{21} Mx, which agrees well with the value above.

The total *vertical* magnetic flux for the whole area at latitudes above 70° is then estimated to be 5.6×10^{21} Mx with the nominal filling factor considered and 2.5×10^{22} Mx with $f = 1$, assuming that the unobserved polar region has the same magnetic flux as that observed with SOT. The estimate taking into account the effect of stray light is 1.8×10^{22} Mx. Here we chose only the flux tubes vertical to the local surface, and the horizontal flux is not included. Since the surface area with latitude above 70° is 1.8×10^{21} cm^2 , the average fluxes are 3.1 G (with the nominal filling factor f considered), 13.9 G (with $f = 1$), and 10.0 G (with 50% of stray light taken into account). Although these are the most accurate flux estimates so far made for the polar regions, the numbers should be regarded as minimum values because of the threshold in the selection of pixels for accurate inversion.

4. KILOGAUSS MAGNETIC PATCHES AND ACCELERATION OF THE FAST SOLAR WIND

4.1. Comparison between Photospheric and Interplanetary Magnetic Flux

The *Hinode* X-ray image taken on 2007 March 16 shows that the apparent polar coronal hole extends down to 60° – 70° in latitude. Thus, the entire region shown in Figure 3 is the photospheric base of the polar coronal hole. We next compare the magnetic flux in the polar photosphere and that observed in interplanetary space during a different solar cycle. The mean magnetic field strength observed by *Ulysses* in 1993–1997 was 2.83 nT (2.83×10^{-5} G) above 36° heliolatitude at 1 AU (McComas et al.

2000), and the total magnetic flux of the polar coronal hole is estimated to be 2×10^{22} Mx, which is somewhat larger than the total photospheric magnetic flux obtained here with our effective filling factor and close to the flux with unity filling factor. We consider these numbers to be consistent, since (1) the actual filling factor must be between 1 and the effective value derived above, (2) there may be smaller undetected vertical flux tubes, as indicated by the presence of spicules, (3) the measurements were made in different solar cycles, and (4) we obtained the photospheric flux at latitudes higher than 70° , whereas the polar coronal hole extends below 70° .

4.2. Polar Flux Tubes and the Fast Solar Wind

The fast solar wind emanates from the polar regions (Krieger et al. 1973; Woch et al. 1997). The vertical flux tubes should undergo a large expansion between the photosphere and the lower corona as a result of their high field strength, the unipolarity, and their very limited number and size in the polar region. The total area S of vertical flux tubes with average field strength $Bf > 200$ G (Fig. 4, *red contours*) is 2.1×10^{18} cm^2 , and the total surface area of the photosphere corresponding to the SOT field of view is 7.2×10^{20} cm^2 . Thus, the areal expansion of individual flux tubes between the photosphere and the lower corona may reach a factor of 345.

The mean number density and velocity in the fast solar wind as observed by *Ulysses* are 2.7 cm^{-3} and 760 km s^{-1} , respectively, at 1 AU and heliolatitudes above 60° . These values exhibit little variation with heliolatitude (McComas et al. 2000). On this basis, we estimate a total mass loss of 2.3×10^8 kg s^{-1} from one of the polar regions, assuming uniform-plasma parameters. The plasma density ρ at $\tau_{5000} = 1$ is 3×10^{-7} g cm^{-3} , and the upward speed associated with a fast solar wind is estimated to be only 2 cm s^{-1} . The apparent Doppler velocity further decreases if one takes into account the projection effect. Indeed, we do not see any velocity feature at the locations of the vertical flux tubes.

In a more mixed-polarity region, a larger fraction of the field lines will return at lower heights, allowing greater expansion for those that are indeed open higher in the corona. But in the polar regions, as soon as the vertical field lines reach the chromosphere or the chromospheric-coronal boundary the fields will expand, since there is no obstacle to lateral expansion of the vertical flux tubes. Horizontal fields, although ubiquitous, would not reach the corona. All the open field lines forming the polar coronal hole essentially originate from such scattered, small, but intense magnetic patches, and the fast solar wind emanates from these vertical flux tubes seen in the photosphere (“magnetic funnels”; Tu et al. 2005).

Alfvén waves are believed to play a vital role in the acceleration and heating of the fast solar wind (Hollweg 1972; Suzuki & Inutsuka 2006). The Alfvén speed rapidly increases with height as a result of the decrease in plasma density. A long-standing problem is that Alfvén waves with wavelengths shorter than the Alfvénic scale height tend to be reflected back (An et al. 1989; Moore et al. 1991). A rapid decrease in the magnetic field strength associated with rapidly expanding flux tubes near the chromospheric boundary would reduce the vertical change in Alfvén speed, resulting in a longer Alfvénic scale height. Therefore, the Alfvénic cutoff frequency may be lower in the polar flux tubes. We thus conjecture that Alfvén waves generated in the photosphere may be more efficiently propagated to the corona through the fanning-out flux tubes. These flux tubes may serve as the chimneys providing the entire coronal hole with Alfvén waves to accelerate solar winds.

5. DISCUSSION

We have discovered that the poloidal field near the south solar pole has the form of unipolar flux tubes scattered throughout the region rather than a weak extended field. If a polar field with the same total magnetic flux $\Phi \sim BfS$ were uniformly distributed (S being the total magnetic area), the estimated effective field strength would be about 10 G, as described above. The total magnetic energy is then proportional to $B^2fS = B\Phi$. Thus, the surface poloidal magnetic energy is approximately 90 times larger than in the case of a uniform magnetic field if we take $B \sim 900$ G, corresponding to the peak of the energy PDF in Figure 5b. The equipartition field strength B_e is that at which the magnetic energy is equal to the kinetic energy of the surface granular motion: $B_e = (4\pi\rho v^2)^{1/2}$. The typical value of B_e is about 400 G for granules with a velocity of $v = 2 \times 10^5$ cm s⁻¹ and the plasma density ρ given in § 4.2. The magnetic field strength for the majority of the patches is larger than the equipartition field strength.

The observed unipolar, strong flux tubes scattered about the polar region are considered to represent seed poloidal fields for toroidal fields (Wang et al. 1989a, 1989b). Magnetic flux is transported to the polar regions by meridional flows and supergranular diffusion in the flux-transport dynamo model (Dikpati & Charbonneau 1999). Since the magnetic field takes the form of such isolated flux tubes with super-equipartition strength instead of the diffuse weak mean field assumed in the flux-transport dynamo (Dikpati & Charbonneau 1999), flux transport on the Sun would occur by means of an aerodynamic (drag) force against the magnetic tension force and may be more difficult than in the mean field case assumed in the models.

If the flux tubes seen on the surface of the Sun are maintained inside the Sun, this would affect a known difficulty in the Ω -mechanism (Elsasser 1956) to generate intense toroidal fields: a smaller amplification factor is needed to generate the same toroidal field from a poloidal field with an intrinsic field strength of 1 kG than from an average 10 G field and thus may be achievable within a solar cycle. We however recognize that there would remain a serious energetics problem if the toroidal field strength indeed reached 100 kG (Schüssler 1996; Rempel 2006).

The total flux of the vertical magnetic field in the polar region estimated here is at most 7.2×10^{21} Mx at solar minimum, while various measurements of the total magnetic flux of single active regions indicate $\sim 10^{22}$ Mx (Longcope et al. 2007; Jeong & Chae 2007; Magara & Tsuneta 2008). Thus, the measured total polar flux scarcely corresponds to that of a single active region. The total toroidal flux would increase with time during the winding-up process by virtue of differential rotation, and the concept of the Ω -mechanism could be viable with the observations presented here.

The transient horizontal magnetic field discovered in the polar region appears to have properties similar to those found in the quiet Sun and in active regions (Lites et al. 2008; Centeno et al. 2007; Orozco Suárez et al. 2007a; Ishikawa et al. 2008; Ishikawa & Tsuneta 2009). In particular, the PDFs of the magnetic field strength for the polar region (Fig. 5a), quiet Sun, and active regions (Ishikawa & Tsuneta 2009) are remarkably similar, suggesting a common local dynamo process (Cattaneo 1999) taking place all over the Sun.

The X-ray telescope and extreme-UV imaging spectrometer aboard *Hinode* have observed remarkable activity in the polar regions in the form of microflares and jets (Savcheva et al. 2007; Cirtain et al. 2007). The lateral spreading of the vertical flux tubes to large areas may occur well above the formation height of the two Fe lines, since there is no clear positional correlation between the horizontal fields and the vertical fields, as seen in Figure 4. These X-ray jets could be due to magnetic reconnection at the lateral magnetic contacts with the horizontal fields or the transient emergence of separate bipolar field lines (Shimojo et al. 1998; Shibata et al. 1992).

In conclusion, the magnetic landscape of the polar region is characterized by vertical kilogauss patches with super-equipartition field strength, a coherence in polarity, lifetimes of 5–15 hr, and ubiquitous weaker transient horizontal fields. The lifetime of the magnetic concentrations in the quiet Sun has been estimated to be 2500 s for 2.5×10^{18} Mx, and 40 ks for 10×10^{18} Mx, with the *SOHO* Michelson Doppler Imager (Hagenaar et al. 1999). It is important to clarify the similarities and differences between the polar region and the quiet Sun with *Hinode*. We will discuss this in a subsequent paper.

S. T. thanks T. Magara, M. Rempel, K. Fujiki, T. Rimmele, T. J. Okamoto, N. Narukage, and R. Ishikawa for fruitful discussions. The authors express sincere thanks to the ISAS/JAXA *Solar-B* launch team, headed by Y. Morita, for their exceptional achievement. *Hinode* is a Japanese mission developed and launched by ISAS/JAXA, collaborating with NAOJ as a domestic partner and NASA and STFC (UK) as international partners. This work was carried out at the NAOJ *Hinode* Science Center, which is supported by the Grant-in-Aid for Creative Scientific Research “The Basic Study of Space Weather Prediction” from MEXT, Japan (Head Investigator: K. Shibata), generous donations from Sun Microsystems, and NAOJ internal funding. The SOT Focal Plane Package of the Lockheed Martin Solar and Astrophysics Laboratory and the High Altitude Observatory was supported by NASA contract NNM07AA01C.

REFERENCES

- An, C.-H., Musielak, Z. E., Moore, R. L., & Suess, S. T. 1989, *ApJ*, 345, 597
 Blanco Rodriguez, J., Okunev, O. V., Puschmann, K. G., Kneer, F., & Sánchez-Andrade Nuño, B. 2007, *A&A*, 474, 251
 Cattaneo, F. 1999, *ApJ*, 515, L39
 Centeno, R., et al. 2007, *ApJ*, 666, L137
 Cirtain, J. W., et al. 2007, *Science*, 318, 1580
 del Toro Iniesta, J. C. 2003, *Introduction to Spectropolarimetry* (Cambridge: Cambridge Univ. Press)
 Dikpati, M., & Charbonneau, P. 1999, *ApJ*, 518, 508
 Durrant, C. J., Turner, J. P. R., & Wilson, P. R. 2004, *Sol. Phys.*, 222, 345
 Elsasser, W. M. 1956, *Rev. Mod. Phys.*, 28, 135
 Gopalswamy, N., Lara, A., Yashiro, S., & Howard, R. A. 2003, *ApJ*, 598, L63
 Hagenaar, H. J., Schrijver, C. J., Title, A. M., & Shine, R. A. 1999, *ApJ*, 511, 932
 Harvey, J. W., Branston, D., Henney, C. J., & Keller, C. U. 2007, *ApJ*, 659, L177
 Hollweg, J. V. 1972, *Cosmic Electrodyn.*, 2, 423
 Homann, T., Kneer, F., & Makarov, V. I. 1997, *Sol. Phys.*, 175, 81
 Ichimoto, K., et al. 2008, *Sol. Phys.*, 249, 233
 Ishikawa, R., & Tsuneta, S. 2009, *A&A*, in press
 Ishikawa, R., et al. 2008, *A&A*, 481, L25
 Jeong, H., & Chae, J. 2007, *ApJ*, 671, 1022
 Kosugi, T., et al. 2007, *Sol. Phys.*, 243, 3
 Krieger, A. S., Timothy, A. F., & Roelof, E. C. 1973, *Sol. Phys.*, 29, 505
 Lin, H., Varsik, J., & Zirin, H. 1994, *Sol. Phys.*, 155, 243
 Lites, B. W. 1996, *Sol. Phys.*, 163, 223
 Lites, B. W., et al. 2008, *ApJ*, 672, 1237
 Longcope, D., Beveridge, C., Qiu, J., Ravindra, B., Barnes, G., & Dasso, S. 2007, *Sol. Phys.*, 244, 45
 Magara, T., & Tsuneta, S. 2008, *PASJ*, in press
 Martínez Pillet, V., Lites, B. W., & Skumanich, A. 1997, *ApJ*, 474, 810
 McComas, D. J., et al. 2000, *J. Geophys. Res.*, 105, 10419
 Moore, R. L., Musielak, Z. E., Suess, S. T., & An, C.-H. 1991, *ApJ*, 378, 347
 Okunev, O. V. 2004, Ph.D. thesis, Univ. Göttingen

- Okunev, O. V., & Kneer, F. 2004, *A&A*, 425, 321
- Orozco Suárez, D., et al. 2007a, *ApJ*, 670, L61
- . 2007b, *PASJ*, 59, S837
- Rempel, M. 2006, *ApJ*, 647, 662
- Savcheva, A., et al. 2007, *PASJ*, 59, S771
- Schüssler, M. 1996, in *Solar and Astrophysical Magnetohydrodynamic Flows*, ed. K. C. Tsinganos (NATO ASI Ser. C, 481) (Dordrecht: Kluwer), 17
- Shibata, K., et al. 1992, *PASJ*, 44, L173
- Shimizu, T., et al. 2008, *Sol. Phys.*, 249, 221
- Shimojo, M., Shibata, K., & Harvey, K. L. 1998, *Sol. Phys.*, 178, 379
- Suematsu, Y., et al. 2008, *Sol. Phys.*, 249, 197
- Suzuki, T. K., & Inutsuka, S. 2006, *J. Geophys. Res.*, 111, No. A06101
- Tang, F., & Wang, H. 1991, *Sol. Phys.*, 132, 247
- Tsuneta, S., et al. 2008, *Sol. Phys.*, 249, 167
- Tu, C.-Y., Zhou, C., Marsch, E., Xia, L.-D., Zhao, L., Wang, J.-X., & Wilhelm, K. 2005, *Science*, 308, 519
- Wang, Y.-M., Nash, A. G., & Sheeley, N. R., Jr. 1989a, *Science*, 245, 712
- . 1989b, *ApJ*, 347, 529
- Woch, J., Axford, W. I., Mall, U., Wilkin, B., Livi, S., Geiss, J., Gloeckler, G., & Forsyth, R. J. 1997, *Geophys. Res. Lett.*, 24, 2885